processes

MDPI

Article

Numerical Simulation of Flame Propagation in a 1 kN GCH4/GO2 Pintle Injector Rocket Engine

Alexandru Mereu and Dragos Isvoranu *

Department of Aerospace Sciences Elie Carafoli, Faculty of Aerospace Engineering, National University of Science and Technology POLITEHNICA Bucharest, 060042 Bucharest, Romania; mru.alexandru@gmail.com
* Correspondence: ddisvoranu@gmail.com

Abstract: Over the last few years, the appeal for using methane as green fuel for rocket engines has been on an increasing trend due to the more facile storage capability, reduced handling complexity and cost-effectiveness when compared to hydrogen. The present paper presents an attempt to simulate the ignition and propagation of the flame for a 1 kN gaseous methane–oxygen rocket engine using a pintle-type injector. By using advanced numerical simulations, the Eddy Dissipation Concept (EDC) combined with the Partially Stirred Reactor (PaSR) model and the Shielded Detached Eddy Simulation (SDES) were utilized in the complex transient ignition process. The results provide important information regarding the flame propagation and stability, pollutant formation and temperature distribution during the engine start-up, highlighting the uneven mixing regions and thermal load on the injector. This information could further be used for the pintle injector's geometry optimization by addressing critical design challenges without employing the need for iterative prototyping during the early stages of development.

Keywords: ignition; pintle injector; GCH4/GO2 rocket engine; EDC; pollutants formation

check for updates

Academic Editor: Jiaqiang E

Received: 17 December 2024
Revised: 31 January 2025
Accepted: 4 February 2025
Published: 6 February 2025

Citation: Mereu, A.; Isvoranu, D. Numerical Simulation of Flame Propagation in a 1 kN GCH4/GO2 Pintle Injector Rocket Engine. *Processes* **2025**, *13*, 428. https://doi.org/10.3390/pr13020428

Copyright: © 2025 by the authors. Licensee MDPI, Basel, Switzerland. This article is an open access article distributed under the terms and conditions of the Creative Commons Attribution (CC BY) license (https://creativecommons.org/licenses/by/4.0/).

1. Introduction

The pintle injector is a type of propellant injector used in rocket engines. Its history dates back to the mid-1950s when Caltech's Jet Propulsion Laboratory (JPL) first developed it to study the mixing and combustion reaction times of hypergolic liquid propellants. In the early 1960s, the pintle injector was further developed by Space Technology Laboratories (STL), later known as TRW, and it was first used in a crewed spacecraft during the Apollo Program's Lunar Excursion Module's Descent Propulsion System. The design was made public in 1972, and U.S. patent 3,699,772 was granted to its inventor, Gerard W. Elverum Jr. Pintle injectors are known for their simplicity and efficiency, offering high combustion efficiency and the ability to implement deep throttling and injector face shutoff. They have been used in various rocket engines, ranging from small thrusters to large engines for spacecraft, including Reusable Launch Vehicles (RLVs) due to their ability to handle deep throttling, which is crucial for controlled landings and take-offs. Their simple design and high performance make them ideal for this purpose. The study of pintle injectors is a hot topic widely popular in recent years [1–4]. Recent studies have focused on optimizing pintle injector designs for Liquid-Propellant Rocket Engines (LPREs) using various propellants like liquid oxygen and gaseous methane. These designs aim to improve performance parameters such as spray angle, vaporization distance, and Sauter mean diameter (SMD) [5–7]. However, research on combustion characteristics of the pintle injector is quite scarce and limited to gaseous methane [8–10].

The reason for which the combustion simulations on engines with pintle injectors are crucial is related to the pintle tip exposure temperature, which could create permanent damage in a very short time. The ablation of the pintle tip could create a catastrophic failure, such as presented by the work of Yibing Chang and Jianjun Zou [11], studying the ablation suffered by a 500 N gaseous engine using a pintle device. In this work, the stainless steel pintle tip suffered extreme ablation due to the chromium precipitates at temperatures over 1273 K. The study was performed on three different O/F mixture fractions: 0.8, 2 and the designed operation condition fraction of 3.2. The numerical simulation was performed using a reduced six-step Jones–Lindstedt mechanism [12], the $k - \varepsilon$ turbulence model and ideal gas density properties, with the thermal conductivity of the pintle tip set to 18.3 W/(m·K). The comparison between the numerical approach and the experimental results showed that a preliminary analysis regarding the thermal load and combustion flow can be used until a higher fidelity model is developed.

V.M. Zubanov et al. [13] present a method for simulating transient combustion in a rocket engine that uses gaseous hydrogen and oxygen. In this paper, three simulation models were studied: the Eddy Dissipation Model (EDM), Finite Rate Chemistry (FRC), and Flamelet combustion model. The results showed that the EDM model can produce quick and qualitative results, although the temperatures obtained from this approach are excessive.

Another issue with using the EDM model in non-stationary simulations is that it does not account for the reaction rates of systems containing multiple reaction steps, meaning the model can only be successfully used for reactions that have two steps. Therefore, the FRC combustion model was addressed, which uses the Arrhenius equation to determine the reaction rate. However, this approach was also unsuccessful. One probable reason for the simulation's volatility was the lack of consistency among the reaction rates, which varied from one reference to another. After implementing reaction models from the work of Gerasimov et al. [14], which provides 26 reaction equations, the stability of combustion still could not be achieved by the authors. The next step was implementing the Flamelet model [15,16]. Using this approach, the authors obtained satisfactory results, solving the problem created by the EDM model, which overestimated the temperature in the combustion chamber. In this model, combustion occurs at the fuel-oxidant mixture front, with a low reaction time, given the presence of unreacted components, as noticed by the authors.

A chemical equilibrium model for a 3D analysis on a liquid propellant rocket engine with a pintle injector was implemented by Youngsung Ko et al. [17], covering the combustion performance and the efficiency of pintle tip cooling. The coupled pressure-based transient simulation was performed using the SRK real gas density model with the $k - \varepsilon$ turbulence model. The chosen method provided similar results to the experimental campaign regarding the temperature distribution on the tip of the pintle injector, even though the chemical equilibrium model overestimated the overall combustion temperature.

In liquid–gas combustion modeling within liquid rocket engines, the implementation of the Discrete Phase Modeling in combination with a species transport model, such as FRC, EDM, FRC-EDM hybrid, or the Eddy Dissipation Concept (EDC) model, enables a complex analysis of the atomization and combustion characteristics of the injector. These include the skip distance in pintle injectors, documented in Fang's work [18]. The study, performed with a single-step reaction mechanism and the EDM transport model, showed that a ratio of 1 between the total length of the pintle in the chamber and its diameter provides the maximum combustion efficiency.

A study covering the formation of a new recirculation zone when a center post radius is implemented into the pintle injector design [19] provided a method of combustion sim-

ulation based on the EDC model, calculating the reaction rates using small-scale eddies generated by turbulent kinetic energy and turbulent dissipation. This approach, combined with a reduced Jones–Lindstedt 6-step mechanism [12], can provide more accurate predictions regarding the flame length and temperature when compared to the PDF approach [20].

The Flamelet Generated Manifold (FGM) methodology, developed by Oijen and de Goey [21], which implements the flamelet model, can consider the transport effects while also reducing the computational time and decreasing enthalpy error to 0.1% when compared to the ILDM error of 9% [22]. The URANS simulation with non-adiabatic-FGM leads to a more accurate prediction of the mixture fraction than published LES model results [22]. The application of the FGM model for the non-premixed and partially premixed flows shows that for a forced ignition, the local temperature can exceed the adiabatic flame temperature due to the preheated vapor observed in a spray ignition simulation. The FGM approach is mostly used for gas–liquid combustion under supercritical conditions [23].

The current research regarding ignition and flame propagation in engines with pintle injectors is quite scarce. To the best of our knowledge, there are only a handful of papers in the open literature on this subject. The most comprehensive study [24] discusses the start-up process for a model LOX/GCH4 engine, describing, mainly from an experimental point of view, the spraying and mixing stage as well as the torch ignition and flame anchoring around the pintle tip. The simulation was only related to LOX spray development.

A second study [25], also experimental, reveals the process of ignition of a GCH4/LOX mixture in the combustion chamber using a pintle injector in less than half a second. The long duration is related to vaporization and mixing delays associated with inhomogeneous two-phase combustion. Only one dominant low-frequency pressure oscillation was apparent, demonstrating the inherent combustion stability of the pintle injector.

Acknowledging the lack of expensive and cutting-edge technology to set up an experimental test bench, our current endeavor is focused only on spark ignition simulation and further flame development for the GOX/GCH4 combustion chamber with a pintle injector of our own design.

The present paper provides contributions to pintle-based liquid rocket engines through the detailed numerical simulation of the flame propagation and ignition in a methane–oxygen rocket engine. The Eddy Dissipation Concept (EDC), along with the Partially Stirred Reactor (PaSR) model and the Shielded Detached Eddy Simulation (SDES), provides a comprehensive analysis of thermal load, flame dynamics and pollutant formation during the start-up stage of the engine, especially when combined with a complete mechanism, GRI-Mech 3.0, providing NOx formation in atmospheric conditions. The future optimization of the injector design, along with the reduced need for iterative prototyping, can be obtained by the analysis of the high-thermal-stress areas and uneven mixing regions. Having in mind the limited availability of the literature focused on transient ignition modeling in pintle-based rocket engines, the findings in this study contribute to further investigations into reliability improvements and performance enhancement.

2. Models and Background Experiments

The motivation for this paper came from the need for deeper introspection into the process of combustion and flame propagation inside a rocket engine equipped with a pintle injector. This compelling urge arose when a group of rocketry enthusiasts, which included one of the authors, tried to test the ignition of a model thruster which ended up in a catastrophic failure. A posteriori analysis of the remains of the engine showed that the ceramic insulator of a misplaced spark generator detached and impacted the throat of the nozzle, leading to failure.

The designed engine was supposed to produce 1 kN of thrust at sea level, with a specific impulse of 273 s, at a chamber pressure of 20 bar and 0.435 kg/s total mass flow rate. The oxygen–fuel mixture ratio used was 3.6.

The only parameter measured from the experiment was the thrust of 950 N. This same engine is part of another work by the same authors [26], aiming to provide a water-based active cooling system on a reduced-scale engine (Figure 1).



Figure 1. Experimental test conducted on the first iteration of the 1 kN gaseous engine.

This new experimental engine (Figure 2) has an improved injection system, comprised of a redesigned static pintle injector, a new location for a high-temperature custom-made spark generator in the upper recirculation zone, providing a constant flux of cold gases to the igniter, as well as the active water-based cooling system mentioned above.



(**a**) (**b**)

Figure 2. (**a**) Section view of the studied 1 kN reduced-scale gaseous rocket engine with the custom spark generator; (**b**) main dimensions of the injector along with the spark generator location (26 mm from the injector axis and 11 mm from the plate).

Apart from previous research [26] that dealt with steady joint combustion and cooling of the thruster, our present investigation aims to discover insights into the ignition process and flame front propagation at engine start-up. The pintle injectors are recognized for their effectiveness in propellant mixing and their ability to deeply control the throttle of a liquid rocket engine. During the years of their usage, there have been no records indicating any combustion instability; moreover, their simple design of only two main elements, along with the advancement of 3D Additive Manufacturing technologies, enabled a more economical approach to the iterative process of liquid rocket engine injector development. The main components of a pintle injector are the central element with a pintle tip, providing radial flow for one of the propellants, and a circumferential annulus, providing axial flow for the other propellant; thus, the two species intersect each other in an impingement point. The

exceptional combustion efficiency and the deep throttling ability, even with 250:1 chamber pressure and 50,000:1 thrust scaling with 25 different propellants [27], provide the pintle injector with functional advantages over other types of injectors. The engine geometry has been determined using the Rocket Propulsion Analysis (RPA v.2.3) software [28] by introducing operating parameters, including the chamber pressure, total mass flow rate, mixture ratio (Table 1) and operating atmospheric conditions. With these inputs, the software computed the chamber's initial dimensions and the exhaust nozzle. The exhaust nozzle has been computed by using the method of characteristics. Due to the increase in demand for sustainable rocket propellants and reusable rocket engines, methane and oxygen were chosen for this engine based on the reduced soot and pollutants production. The alternative proposed variant was hydrogen, but the higher combustion temperature and storage difficulty proved to be too expensive, for now, in this research. Another reason for choosing methane and oxygen in a gaseous state of matter is linked to the purpose of this engine, being an improved follow-up to the first prototype.

Table 1. Engine parameters.

Parameter	Values at Sea Level
Thrust (N)	1000
Chamber pressure (MPa)	2
O/F ratio	3.6
Oxidizer injection temperature (K)	300
Fuel injection temperature (K)	450
Specific impulse (s)	273
Total mass flow rate (kg/s)	0.435

3. Numerical Methodology

3.1. Shielded Detached Eddy Simulation (SDES) Model

This model is an advanced hybrid RANS-LES approach for turbulent flows designed for wall-bounded flows with high Reynolds numbers. The SDES model [29] (p. 111) is based on the Delayed Detached Eddy Simulation (DDES) framework [30] (p. 1006), handling turbulent flows by using both the RANS approach, at the boundary layer regions and the LES approach for the detached flows.

The RANS model used for the SDES turbulence model is the Shear Stress Transport SST (k-ω), governed by the following transport equations:

$$\frac{\partial}{\partial t}(\rho k) + \frac{\partial}{\partial x_i}(\rho k u_i) = \frac{\partial}{\partial x_j}\left(\Gamma_k \frac{\partial k}{\partial x_j}\right) + G_k - Y_k + S_k \quad (1)$$

and

$$\frac{\partial}{\partial t}(\rho \omega) + \frac{\partial}{\partial x_i}(\rho \omega u_j) = \frac{\partial}{\partial x_j}\left(\Gamma_\omega \frac{\partial \omega}{\partial x_j}\right) + G_\omega - Y_\omega + D_\omega + S_\omega \quad (2)$$

in which ρ is density, k is the turbulent kinetic energy, ω is the specific dissipation rate G_k is the turbulence kinetic energy generation, G_ω is the generation of ω, Γ_k and Γ_ω are the effective diffusivity of k and ω, Y_k and Y_ω are the dissipation due to turbulence of k and ω, S_k and S_ω are source terms defined by the user and the buoyancy terms are accounted for by G_k and G_ω.

The first step in obtaining SDES starts with the DDES-SST model, in which the dissipation of the turbulent kinetic energy is modified for the DES model:

$$Y_k = \rho\beta^* k\omega F_{DES} \tag{3}$$

in which β^* is a model constant, and F_{DES} is

$$F_{DES} = max\left(\frac{L_t}{C_{des}\Delta_{max}}, 1\right) \tag{4}$$

The SDES introduces a shielding function preventing premature LES switching at the RANS boundary layer while also improving the grid length scale definition for a smoother RANS to LES transition. The SDES formulation in two-equation models is attained by modifying the sink term in the k equation. For SST, the modification brings the addition of a dissipation rate term defined below:

$$\varepsilon_{SDES} = -\beta^*\rho k\omega F_{SDES} \tag{5}$$

where F_{SDES} is the specific SDES blending function:

$$F_{SDES} = \left[max\left(\frac{L_t}{C_{SDES}\Delta_{SDES}}(1 - f_{SDES}), 1\right) - 1\right] \tag{6}$$

L_t is the turbulent length scale, C_{SDES} is a calibration parameter for the RANS to LES transition, f_{SDES} is a blending function controlling how much of the flow is treated as RANS and how much as LES; it has a range between 0 and 1. When the value is 1, the model is using RANS, while at a value of 0, it behaves like LES. $max\left(\frac{L_t}{C_{SDES}\Delta_{SDES}}(1 - f_{SDES}), 1\right)$ determines the blending level between RANS and LES, assuring that the switch is not made to LES if it is not appropriate. Δ_{SDES} is the mesh length scale for the SDES model:

$$\Delta_{SDES} = max\left(\sqrt[3]{Vol}, 0.2\Delta_{max}\right) \tag{7}$$

in which Vol is the control volume in the mesh cell and Δ_{max} is the maximum grid spacing.

3.2. Eddy Dissipation Concept (EDC)

The nature of the simulation implies a transient formulation during the ignition process consisting of running the whole simulation as a time-dependent method, which also provides a more precise visualization of the injection flow, as well as a more precise timing for the ignition, preventing detonation. The combustion process generated with the pintle injector can be very well circumscribed in partially premixed combustion environments, which represents a combination of non-premixed (diffusion) and premixed combustion systems. The non-premixed combustion occurs primarily near the pintle tip, where the mix of the fuel and oxidizer is predominantly accomplished by turbulent diffusion, while the premixed combustion is mostly developed downstream in regions where the recirculation zones and turbulence promote a more thorough mixing of the reactants, thus creating a hybrid flame structure.

The species transport is governed by the following conservation equation [29] (p. 222):

$$\frac{\partial}{\partial t}(\rho Y_i) + \nabla\cdot\left(\rho\vec{v}Y_i\right) = -\nabla\cdot\vec{J_i} + R_i + S_i \tag{8}$$

Herein, $\vec{J_i}$ is the mass diffusion, Y_i is the mass fraction of the species, $\vec{v}$ is the velocity of the fluid flow and R_i is the source term. For turbulent flows, the mass diffusion is computed by Ansys Fluent in the following way [29] (p. 222):

$$\vec{J_i} = -\left(\rho D_{i,m} + \frac{\mu_t}{Sc_t}\right)\nabla Y_i - D_{T,i}\frac{\nabla T}{T} \tag{9}$$

in which $D_{i,m}$ is the species mass diffusion coefficient for i in the mixture, μ_t is the turbulent viscosity, $D_{T,i}$ is the thermal diffusion coefficient, Y_i is the local mass fraction of the species and Sc_t is the turbulent Schmidt number (0.7 in this case).

As an extension to the Eddy Dissipation Model (EDM), EDC also includes finite-rate chemical reactions by accounting for a slower reaction time than the one given by turbulent mixing, while EDM assumes that the chemical reaction is instantaneous. The EDC model calculates the reaction rates in the small-scale eddies accounting for the eddy residence time. While EDM calculates the reaction rate by comparing the availability of reactants and the turbulent dissipation rate and using whichever is lower from the two, EDC defines the source term as follows:

$$R_i = \rho k \frac{Y_i^* - Y_i}{\tau^*} \tag{10}$$

where Y_i^* denotes the species mass fraction at the finite scale after undergoing reactions over the time scale $\tau*$. The molar rate of creation or destruction of species i in the rth reaction of the chemical mechanism following Arrhenius form is expressed as

$$\hat{\mathrm{R}}_{i,r} = \Gamma\left(v''_{i,r} - v'_{i,r}\right)\left(k_{f,r}\prod_{j=1}^{N}\left[C_{j,r}\right]^{\eta'_{j,r}} - k_{b,r}\prod_{j=1}^{N}\left[C_{j,r}\right]^{\eta''_{j,r}}\right) \tag{11}$$

Here, Γ is the net effect of third bodies on the reaction rate, $C_{j,r}$ is the molar concentration of species, $\eta'_{j,r}$ is rate exponent for reactant species j in reaction r, $\eta''_{j,r}$ is the rate exponent for product species, $k_{f,r}$ is the forward rate constant, $k_{b,r}$ is the backward rate constant, with $v'_{i,r}$ and $v''_{i,r}$ being the stoichiometric coefficients for reactant and, subsequently, product.

Since in the standard EDC model, the length scale constant C_{ξ} and the time scale constant C_{τ} do not depend on the chemistry variables or local flow; in certain conditions in which slow chemistry is taking place due to strong oxygen dilution, the model greatly overestimates the temperature magnitude [23]. In attempting to fix this overestimation, a combination of the EDC model with the Partially Stirred Reactor (PaSR) has been studied in several papers, being applied to both supersonic and mild combustions [31,32]. This approach differs from the standard EDC model by an alternative definition of the time scale and reacting volume fraction:

$$k = \frac{t_c}{t_c + t_{mix}} = \frac{1}{1 + Da} \tag{12}$$

$$\tau^* = Min(t_c,\ t_{mix}) \tag{13}$$

where Da is the Damköhler number:

$$Da = \frac{t_{mix}}{t_c} \tag{14}$$

Ansys Fluent computes the chemical time scale t_c based on the reaction rates ω_i of CH_4, CO_2, O_2, H_2O and H_2

$$t_c = max\left(\frac{\rho y_i}{\omega_i}\right) \tag{15}$$

while the mixing time scale t_{mix} is expressed as a fraction of the turbulence integral time scale $t_{mix} = C_{mix}k/\varepsilon$, where C_{mix} is a function of the local turbulent Reynolds number.

The mechanism used is the detailed GRI-Mech 3.0 [33], developed mostly for the combustion of hydrocarbon fuels, primarily for methane, providing great insight regarding the formation of pollutants and flame behavior due to the inclusion of the important HO_2, CH_3, O and OH radicals. Even if the main application for GRI-Mech 3.0 remains methane–air combustion, the incorporation of reburn chemistry and NO formation provides an important evaluation of pollutant formation during start-up, emphasizing the need to develop environmentally sustainable propulsion systems. Even if skeletal mechanisms are more computationally efficient and potentially more suitable for methane–oxygen combustion, the transient ignition process could benefit more from the GRI-Mech 3.0 detailed chemical pathway by noticing that the ignition process in atmospheric conditions takes place in the presence of nitrogen, which most skeletal mechanisms do not use. A comparison and trade-off analysis between the skeletal mechanism and the current mechanism regarding the accuracy and computational cost could be explored in future work.

3.3. Peng–Robinson Real Gas Model

As the pressure in the combustion chamber increases during the ignition process, the properties of the gases start to deviate from the ideal gas behavior, experiencing non-ideal compressibility. For this reason, a real gas model, using cubic equations of state (EOS) like Peng–Robinson, could better predict the enthalpy, entropy, and density of the products, leading to a more accurate representation of the flame propagation. The Peng–Robinson real gas model uses the same general cubic equation of state employed by most of the other models:

$$P = \frac{RT}{V - b + c} - \frac{\alpha}{(V^2 + \delta V + \varepsilon)} \tag{16}$$

In which P is the absolute pressure, V is the specific molar volume, T is the temperature, R is the universal gas constant and the α, b, c, δ and ε are coefficients given for each equation. In the Peng–Robinson model, $\delta = 2b$, $\varepsilon = -b^2$ and $c = 0$. The three necessary parameters required for using the model are the critical temperature T_c, the critical pressure P_c and the acentric factor ω. In this case, as the Peng–Robinson cubic equation of state is used, the specific coefficients are defined using the three required parameters as follows:

$$\alpha_0 = \frac{0.45724 R^2 T_c^2}{P_c} \tag{17}$$

$$b = \frac{0.07780 R T_c}{P_c} \tag{18}$$

where the temperature dependence of α is given by the following function, also used in the Soave–Redlich–Kwong Equation:

$$\alpha(T) = \alpha_0 \left[1 + n \left(1 - \left(\frac{T}{T_c} \right)^{0.5} \right) \right]^2 \tag{19}$$

in which n, specific to the Peng–Robinson EOS, is

$$n = 0.37464 + 1.54226\omega - 0.26992\omega^2 \tag{20}$$

3.4. Spark Model

Spark ignition represents a very complex phenomenon involving plasma kinetics, fluid dynamics, chemical kinetics and molecular transport. It also poses a lot of mathematical difficulties due to the stiff nature of all these processes. The spark model works by introducing

a localized heat source in a user-defined location and converting instantaneously, within a limited number of cells, the unburned reactants into combustion products. The species composition and the temperature are calculated every time step by using the equilibrium burn composition φ^b and the unburned composition φ^u:

$$\varphi = c\varphi^b + (1-c)\varphi^u \tag{21}$$

The radius of the spark increases in time according to [28] (p. 396):

$$\frac{dr}{dt} = \frac{\rho_u}{\rho_b} S_t \tag{22}$$

in which ρ_u is the density of the unburned fluid ahead of the flame front, ρ_b is the density of the burnt fluid behind the flame, and S_t is the turbulent flame speed. In this paper, the turbulent length model was chosen, ignoring the flame curvature effects applied to the flame speed, and it is as follows:

$$S_t = max(S_l, S_t(r)) \tag{23}$$

where r is the spark radius at the given moment. The spark sphere radius is calculated as follows:

$$r_t = max\left(r_0 + 3\Delta,\ 3r_0, min\left(\frac{1}{2}l_t, r_0 + 10\Delta\right)\right) \tag{24}$$

This equation is used to ensure that the volume of the sphere is not too large or too small relative to the cell size. Here, r_0 is the initial spark radius, defined by the user, Δ is the cell length scale and l_t is the turbulent length scale. When the dimension of the spark reaches the turbulent length scale, Ansys Fluent switches off the spark flame model, and it is replaced by the selected model in the species settings, governed by the Zimont model [34] (p. 1035), [35] (p. 1035), [36] (p. 1036), based on the assumption that equilibrium small-scale turbulence exists in the laminar flame, leading to a turbulent flame speed expression written using only large-scale turbulent parameters:

$$S_t = A\left(u'\right)^{3/4} S_l^{1/2} \alpha^{-1/4} l_t^{1/4} \tag{25}$$

$$S_t = MAX\left(S_l, Au'\left(\frac{\tau_t}{\tau_c}\right)^{1/4}\right) \tag{26}$$

in which A is the model constant, u' is the RMS velocity, α is the unburnt thermal diffusivity, τ_t is the turbulence tie scale and τ_c is the chemical time scale. This is applicable when the Kolmogorov scale is smaller than the flame thickness and penetrates in the flame, defined as the reaction zone combustion zone, determined by Karlovitz number:

$$Ka = \frac{t_l}{t_\eta} = \frac{v_\eta^2}{U_l^2} \tag{27}$$

where t_l is the characteristic flame scale, t_η is the Kolmogorov turbulence time scale and v_η is the Kolmogorov velocity.

4. Computational Approach

The computational approach is performed in two steps. In the first step we assess that the numerical scheme is error-free, and it converges on any given domain discretization assuming steady state. Subsequently, we choose the mesh density. In the second step, we move to a transient simulation to capture ignition and flame propagation on the chosen

grid. The numerical schemes used herein are second-order upwind for pressure, density, momentum, energy, turbulence and species. The type of solver used was pressure-based, using the SIMPLE algorithm for pressure–velocity coupling. A Prandtl number equal to 0.85 was considered, and a unity Courant number was used for the transient simulation. The 30° wedge axisymmetric configuration of the combustion chamber presented in Figure 2 is connected to a corresponding ambient control volume outside the combustion chamber just for the purpose of having a precise location for the reference pressure. The meridional mid-plane section of this combined domain is illustrated in Figure 3.

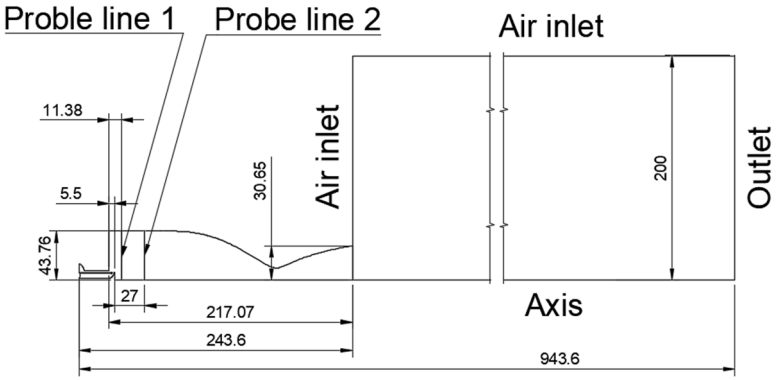


Figure 3. Main dimension of the computation domain in the mid-plane of the 30° wedge configuration.

The main boundary conditions for both simulation steps are illustrated in Table 2.

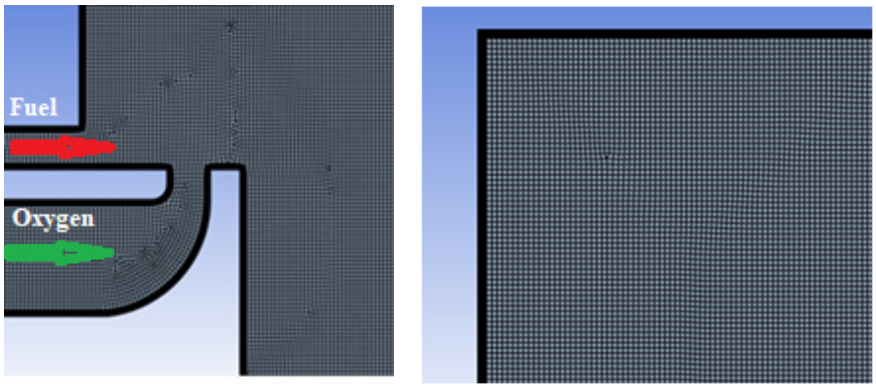
Table 2. Boundary conditions.

Boundary Surface	Boundary Type	Main Value
Inlet fuel	mass flow inlet	0.09454 kg/s
Inlet oxygen	mass flow inlet	0.34043 kg/s
Air inlet	pressure inlet	0 Pa gauge
Outlet	pressure outlet	0 Pa gauge
Solid Walls	wall	adiabatic
Wedge lateral surfaces	periodic	-

The reference pressure for the computational domain is the atmospheric pressure of 101,325 Pa. Temperatures of the fuel and oxygen flows are 450 K and 300 K. The composition structure for air was 76.6% nitrogen and 23.4% oxygen. All domains were initialized at a gauge pressure equal to 0, with mass fractions of 23.4% for oxygen and 76.6% for nitrogen at a temperature of 300 K. For this research, no radiation has been accounted for.

Regarding the material properties, the laminar flame speed needed to compute the spark evolution was chosen as a constant with a value of 0.4 m/s. It is acknowledged that a constant value for the laminar flame is debatable, but the current EDC implementation complicates the introduction of the laminar flame speed by making it dependent on unburnt mixture temperature, pressure and equivalence ratio. Anyway, recent investigations on CH_4/O_2 mixtures are still not able to produce reliable values for the laminar flame speed at high pressures for rocket engine applications [37].

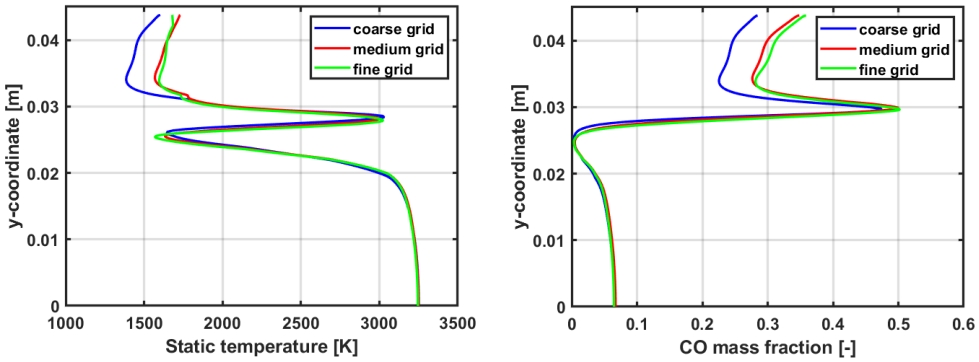
For the first step (mesh-independence test), the domain was meshed with different resolutions following a quadrilateral dominant strategy to obtain an almost complete rectangular grid, which is depicted in Figure 4a,b.



(**a**) (**b**)

Figure 4. Mesh structure at (**a**) the injector region and (**b**) the chamber upper-left corner.

Due to the very fine grid size, only the most relevant details have been presented, reflecting the rectangular shape and inflation layers near the walls. Element sizes ranging from 0.3 to 0.12 mm have been used to obtain grids only in the combustion chamber, counting from $2 \cdot 10^5$ cells on the coarse grid to $8 \cdot 10^5$ cells on the fine grid. The medium grid has $4 \cdot 10^5$ elements. Temperature and carbon monoxide mass fractions have been chosen to demonstrate the grid-independence property of the solutions. The results presented in Figure 5 along the vertical probe line 1 (see Figure 3) show a very good correlation among the three grids. Notice that along this line, very high gradients are expected for all quantities of interest, making it suitable for a more realistic comparison.



(**a**) (**b**)

Figure 5. Probe line profiles: (**a**) static temperature, (**b**) CO mass fraction.

An assessment of the goodness of the solution for the three grids is presented in Table 3. Given that, between the solution on the medium grid and the solution on the fine grid, the maximum differences are below 3%, it was decided to choose the medium grid inside the combustion chamber for further transient analysis. The overall structured mesh contains 793,879 cells.

Table 3. Comparison of the maximum differences of the analyzed parameters among the three grids along probe line 1.

	Coarse Grid		**Medium Grid**		**Fine Grid**	
	Value [K]/[-]	**Diff w.r.t to Fine Grid [%]**	**Value [K]/[-]**	**Diff w.r.t to Fine Grid [%]**	**Value [K]/[-]**	**Diff w.r.t to Fine Grid [%]**
Temperature	1398.4	13.19	1574.9	2.23	1610.8	0
CO Mass fraction	0.2842	20.79	0.3480	3.01	0.3588	0

Once this test has been passed, we can move to the second step of the computation, which is the unsteady simulation. The simulation was performed using an adaptive time-step methodology [38] (p. 3646). In this case, the time step size is proportional to the characteristic time taken for the fluid to cross a control volume and the given Courant number. For convection dominated and/or wave propagation problems, it is recommended to set CFL close to 1 to obtain more accurate results. Usually, the characteristic time scale is taken to be the minimum overall control volume time scale. The adaptive strategy starts with an initial time step, which, during the computation, can be changed based on multiplication with some step size factors ranging between 0.75 and 2 to ensure the time step falls between a minimum and a maximum prescribed value and the CFL number remains close to the value set by the user.

The spark igniter is located 11 mm from the rear vertical chamber wall and 26 mm from the symmetry axis in the mid-plane. The spark adds no energy to the flow. The thermo-chemical state behind the spark flame front is instantaneously equilibrated as the spark propagates, and the burnt temperature is the equilibrium temperature [29] (p. 396). A cold flow was run for 1 ms to allow a small fraction of fuel and oxidizer to enter the chamber so detonation can be prevented during the ignition. After the 1 ms cold flow time, the spark was initialized and ran for 0.5 ms.

5. Results

The results presented below (Figures 6–16) are related to the time flowing from the moment of ignition. The flame front velocity can be estimated based on the propagation between the ignition starting time (Figure 6a) and 0.1 ms after it by measuring the distance the flame traveled during this time. The flame propagated 0.01853 m (18.53 mm) in 0.1 ms (Figure 6b), resulting in a flame front speed of 185.3 m per second during the ignition for a gauge pressure of 0 Pa and a still consistent amount of air inside the chamber. In this way, the choice of 0.4 m/s option for the laminar flame speed can be explained. The turbulent flame speed obtained is consistent with values obtained in similar simulations using the FGM model. Efficient ignition is indicated by the rapid rise in temperature due to the pintle injector mixing properties.

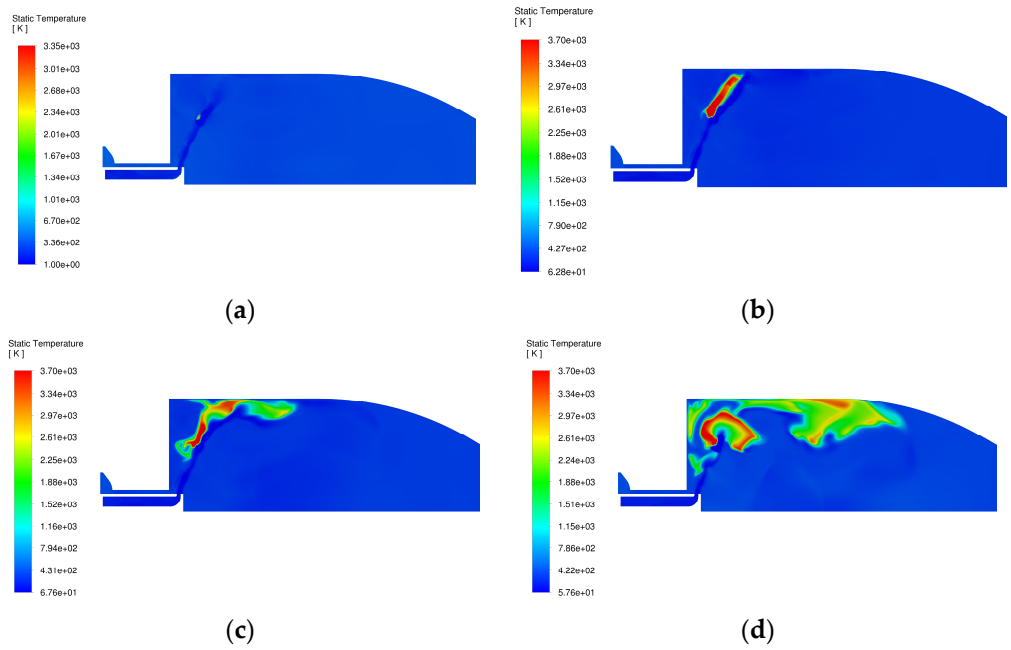
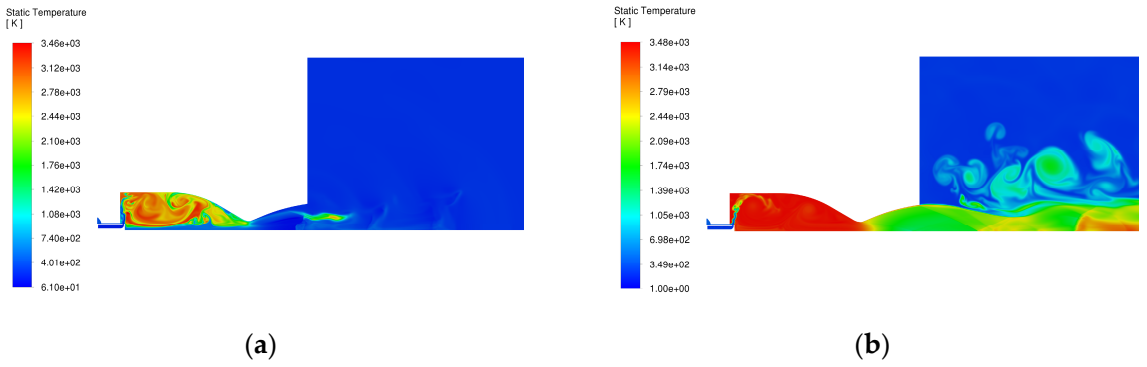
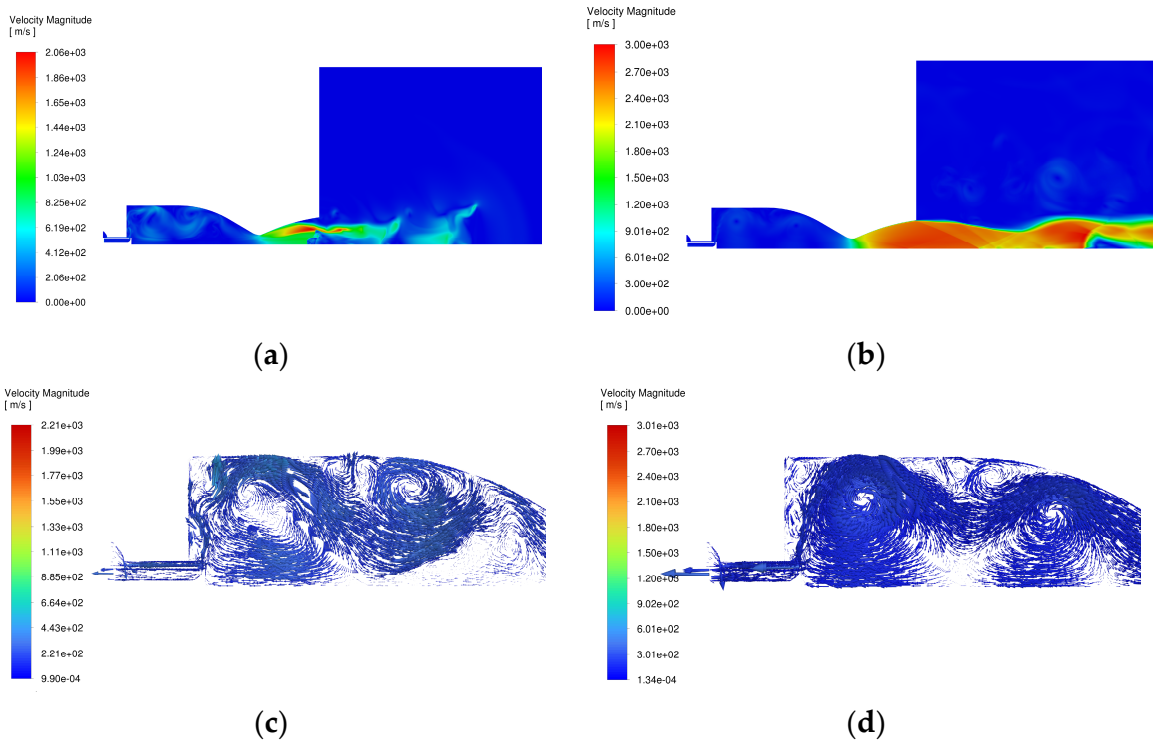


Figure 6. Instantaneous temperature distribution during the first 0.3 ms after initiation of the spark (**a**) 0 ms, spark is initialized; (**b**) 0.1 ms; (**c**) 0.2 ms; (**d**) 0.3 ms.



(**a**) (**b**)

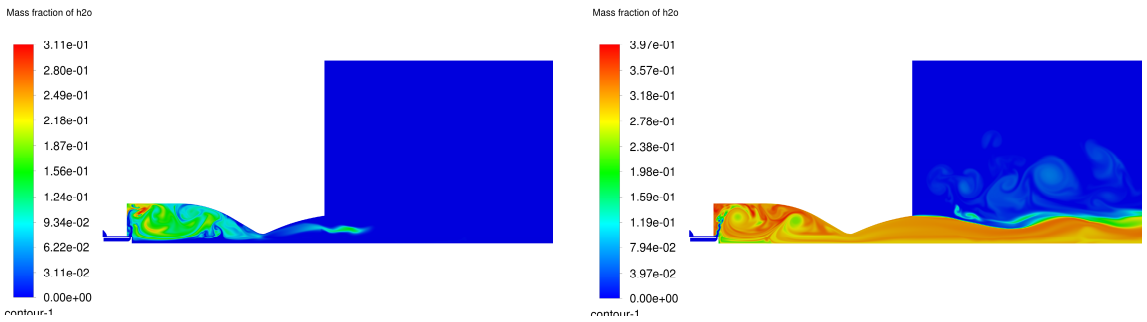
Figure 7. Instantaneous temperature distribution. (**a**) 1 ms; (**b**) 6 ms.



(**a**) (**b**)

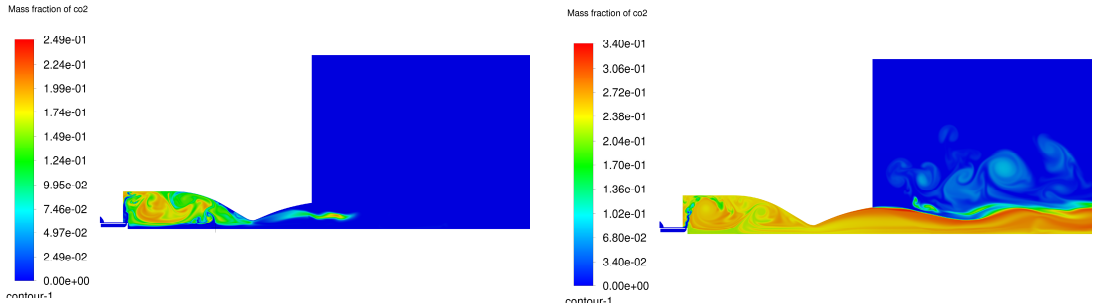
(**c**) (**d**)

Figure 8. Instantaneous velocity magnitude distribution. (**a**) 1 ms; (**b**) 6 ms; (**c**) velocity vectors at 1 ms; (**d**) velocity vectors at 6 ms.



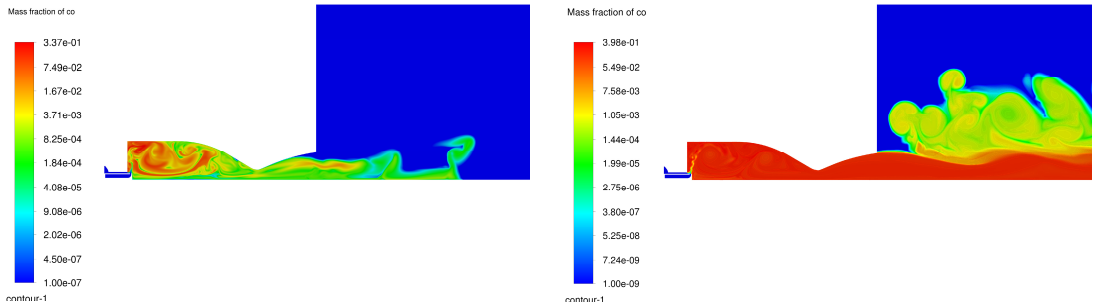
(**a**) (**b**)

Figure 9. Instantaneous water vapor distribution. (**a**) 1 ms; (**b**) 6 ms.



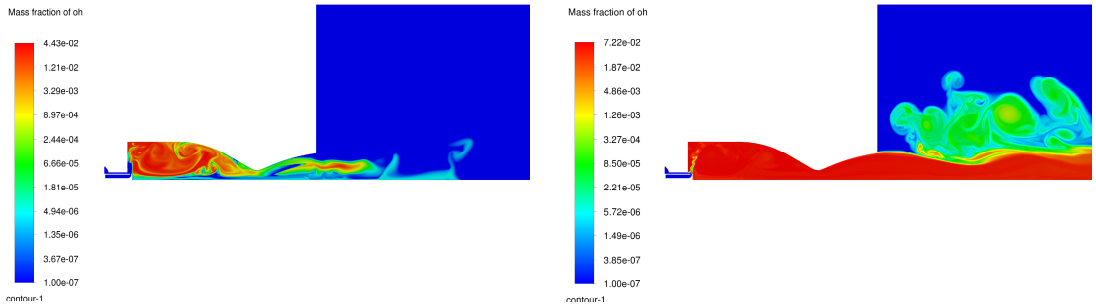
(**a**) (**b**)

Figure 10. Instantaneous carbon dioxide distribution. (**a**) 1 ms; (**b**) 6 ms.



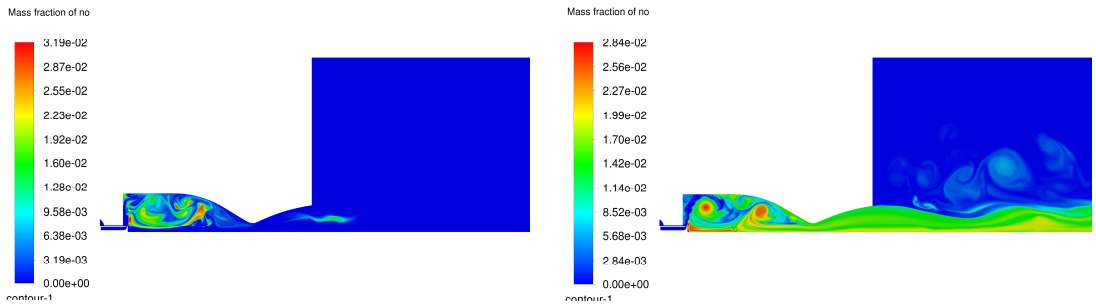
(**a**) (**b**)

Figure 11. Instantaneous carbon monoxide distribution (logarithmic scale). (**a**) 1 ms; (**b**) 6 ms.



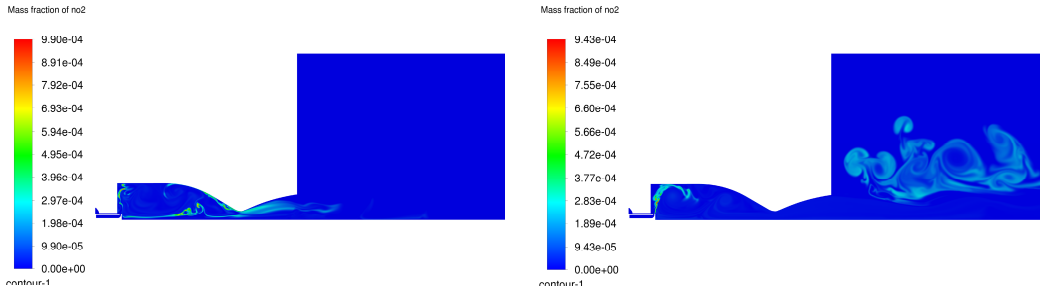
(**a**) (**b**)

Figure 12. Instantaneous hydroxyl radical distribution (logarithmic scale). (**a**) 1 ms; (**b**) 6 ms.



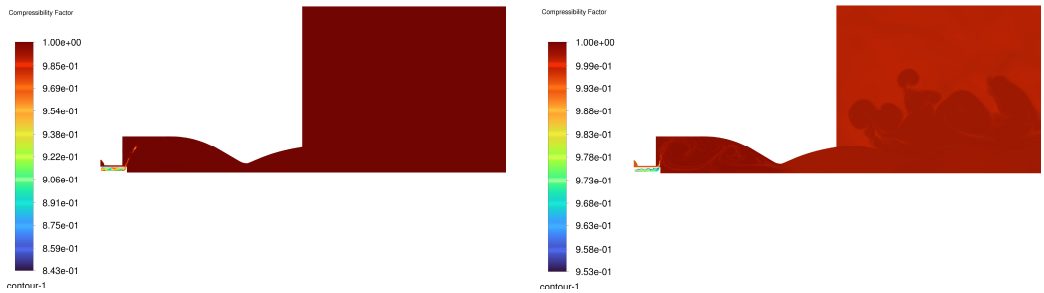
(**a**) (**b**)

Figure 13. Nitric oxide distribution. (**a**) 1 ms; (**b**) 6 ms.



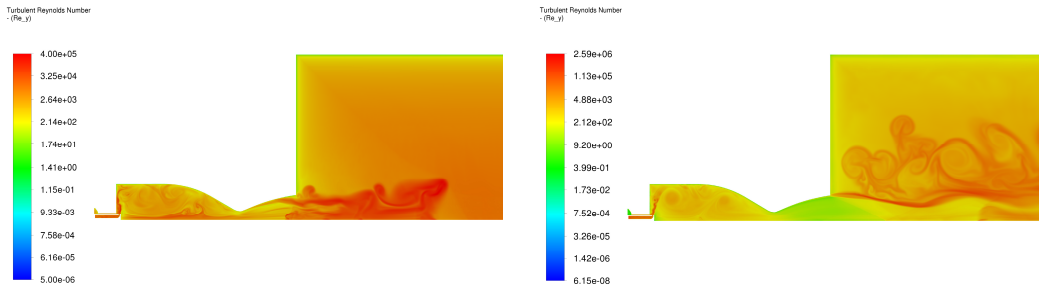
(**a**) (**b**)

Figure 14. Instantaneous nitrogen dioxide distribution. (**a**) 1 ms; (**b**) 6 ms.



(**a**) (**b**)

Figure 15. Compressibility factor. (**a**) 1 ms before ignition; (**b**) 6 ms.



(**a**) (**b**)

Figure 16. Turbulent Reynolds number. (**a**) 1 ms; (**b**) 6 ms.

During the first instances of the ignition process, the flame front is advected along the spray cone (Figure 6b), and then it spreads on the upper wall forward and backward (Figure 6c). The main vortex downstream of the pintle produces bending of the flame front, and burnt gases start approaching the injector to sustain combustion (Figure 6d). It has been remarked that all along the spark duration, the instantaneous maximum value for temperature overshoots the adiabatic flame temperature (~3440 K). This effect is the consequence of the temperature conditions behind the spark introduced by turbulent flame velocity (Equation (25) or Equation (26)) that modifies the source term in the energy equation. Once the spark is switched off, the maximum temperature does not go beyond the adiabatic temperature. The instantaneous evolution of various field distributions for temperature, velocity and the main species of interest H_2O, CO_2, CO, OH, NO and NO_2 are depicted in the following snapshots for two different time stamps, 1 ms and 6 ms, from the initiation of the spark.

According to Figures 6 and 7, it can be stated that the location of the spark very close to the mixture spraying cone is beneficial and works to create a stable combustion zone and efficient flame propagation, leading to continuous combustion. The temperature stabilization downstream (Figure 7b) indicates that the flame is fully developed. Within the

given assumptions, we notice a consistent thermal load exerted on the outer wall of the pintle.

The recirculation zones are produced during the first ms of the flow (Figure 8c,d), increasing the flame stability by extending the residence time and increasing the thorough mixing of the reactants. The results obtained show that these zones improve the fuel–oxidizer reaction, actively producing a stable combustion process. The mixing of the reactants is promoted by the widespread range of gas flow speeds inside the turbulent recirculation zone.

It can be observed that during the first time steps of the ignition process, both the carbon dioxide and water vapor are retained inside the chamber due to the developed recirculation zones. Once the temperature and pressure increase, the products are accelerated through the nozzle. Recirculation of these products for a certain time inside the chamber can lead to maximizing the combustion efficiency.

The highest rate of carbon monoxide production mostly occurs near the mixture spraying cone (Figure 11a,b) due to incomplete carbon oxidation because of relatively low local temperature concurrent with uneven mixing. Once CO is recirculated to higher temperature zones, it will be converted to CO_2. As can be seen from Figure 11b, this is a slow process, taking more time than the time for convection through the nozzle and downstream outside the environment. This also shows that the recirculation zones do not sufficiently increase the residence time for CO/CO_2 conversion. The slowing down of the CO/CO_2 conversion is more pronounced as the burnt gases cool down after passing the throat of the nozzle. Obviously, this represents a loss of available energy, loss of combustion efficiency and maybe a further objective for combustion chamber and pintle optimization.

The fast hydroxyl radical production follows the areas of high reaction rates, where higher temperatures accelerate its formation. This also shows a well-sustained flame, enhanced by the pintle's injector promotion of flame propagation through radical generation. Part of the OH is convected through the nozzle and starts depleting mostly due to temperature drop leading to reaction mechanism termination.

The growing concern regarding the environmental impact of pollutants also concerns the development of space propulsion, with international emphasis increasing on green propulsion systems. Thus, an analysis was performed on the NOx production inside the chamber since the presence of these products is a consequence of nitrogen presence in the initial stage of ignition in the chamber. Even if the flow of the fuel–oxidizer mixture will push most of the initial air outside the chamber, there will still be a sensible amount of air trapped inside the chamber at the inception of combustion. The nitric oxide distribution looks very similar to the hydroxyl radical distribution, at least in the first ms from ignition (Figure 13a). Then, once the temperature has settled, the flame inside the chamber will continue to produce nitric oxide until the exhaustion of nitrogen. Contrary to the distribution of NO, the production of NO_2 resides mostly outside the combustion chamber, where nitric oxide reacts with the oxygen present in the atmosphere, suggesting that it is mostly an external effect (Figure 14b).

The picture above shows the change in the compressibility factor distribution inside the combustion chamber at two different flow times, 1 ms before the ignition and 6 ms after the ignition. The zones in which the compressibility factor is below unity represent areas where gases depart from the ideal gas model. This is mostly visible in Figure 15a, before ignition, near the mixing cone and injector, where the compressibility factor is well below 1, suggesting increased intermolecular forces. Conversely, in Figure 15b, the compressibility factor is close to 1 in most regions where the temperature has increased substantially due to the combustion process. Still, deviations are persisting in areas with

intense turbulent mixing. Thus, the use of real gas models, such as the Peng–Robinson EOS, plays a significant role in determining injector performances.

The increased mixing areas near the injector, highlighted by the high turbulent Reynolds number, imply that the injector induces turbulence effectively, stabilizing the combustion, a very well-known characteristic of the pintle-type injector. The unburned hydrocarbon mass fraction reduction is also promoted through the induced turbulence by increasing their residence time inside the chamber. On the other hand, at later moments, the turbulent shear layer develops outside the nozzle (Figure 15b) and leads to the dispersion of the species (Figures 9b, 10b, 11b, 12b, 13b and 14b) above the jet discharge.

The chemical time scale of the reaction (Figure 17), as determined using the EDC-PaSR model (Equation (15)), can be observed in a snapshot taken at 2.2 ms flow time (after the ignition), in which the small-time scales show the fast reaction rates, while the longer time scale represents the slower reaction rates. Observing that in most of the combustion chambers, the chemical time scale is small, combined with the high values of the turbulent Reynolds number (Figure 16), it becomes apparent that flamelet-based turbulence–chemistry interaction models might be an appealing alternative.

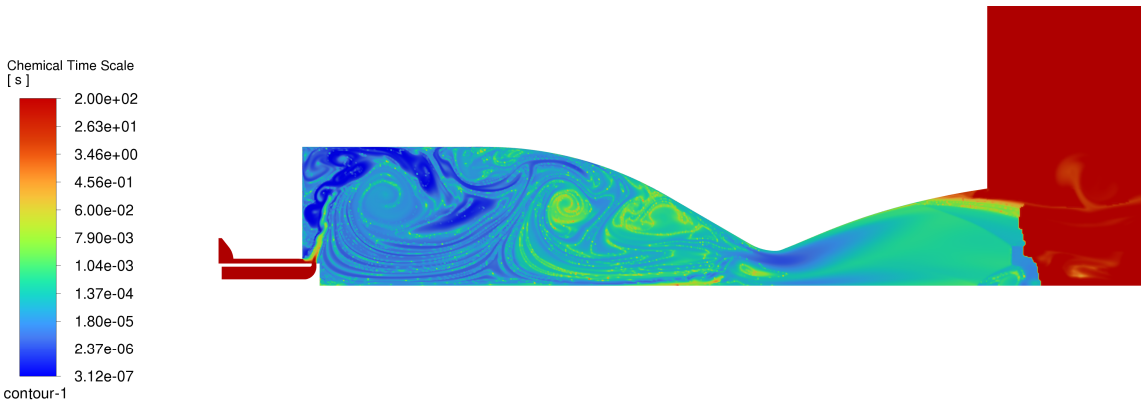


Figure 17. Chemical time scale of the reaction (EDC-PaSR model) at 2.2 ms flow time.

The following graph (Figure 18) shows the variation in the primary species, pressure and temperature with respect to flowtime in the exit section of the nozzle.

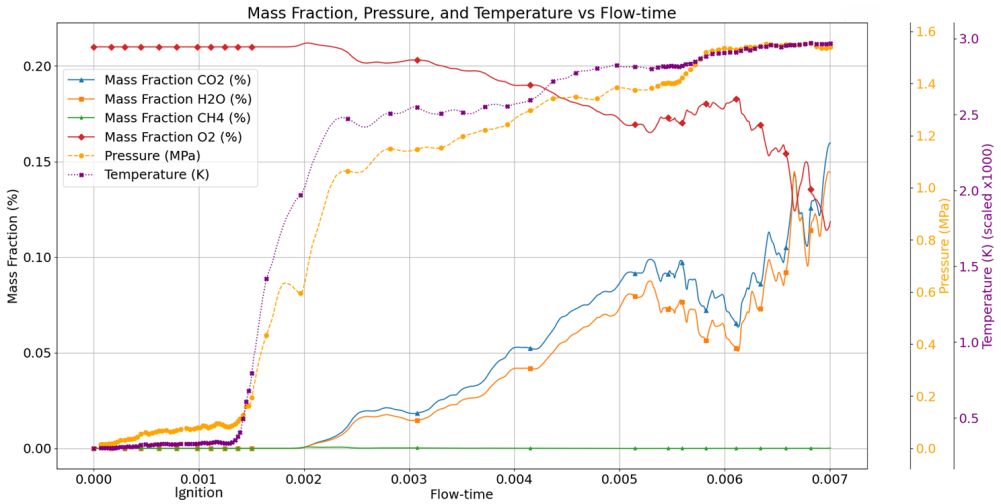


Figure 18. Time history of the instantaneous area-averaged mass fraction, pressure and temperature at nozzle exit.

The temporal evolution of the primary species and combustion conditions in the ignition process provide–indications regarding the trend of the flame front, which proves to be stable, with the CO_2 and H_2O concentrations rising sharply immediately after the ignition and stabilizing when getting closer to the steady state combustion.

The species distribution along probe line 2 inside the combustion chamber can be observed in Figures 19 and 20 at the same time stamps (1 and 6 ms). The illustrated profiles reflect a better introspection in the main recirculation zones in the mid-region of the chamber. At 6 ms, once the recirculation zones reach a mature state, an increase in the number of product species and a sensible decrease in nitrogen concentration is noticed. This shows that the recirculation region is efficient in increasing the residence time of the reactants, thus increasing the combustion efficiency.

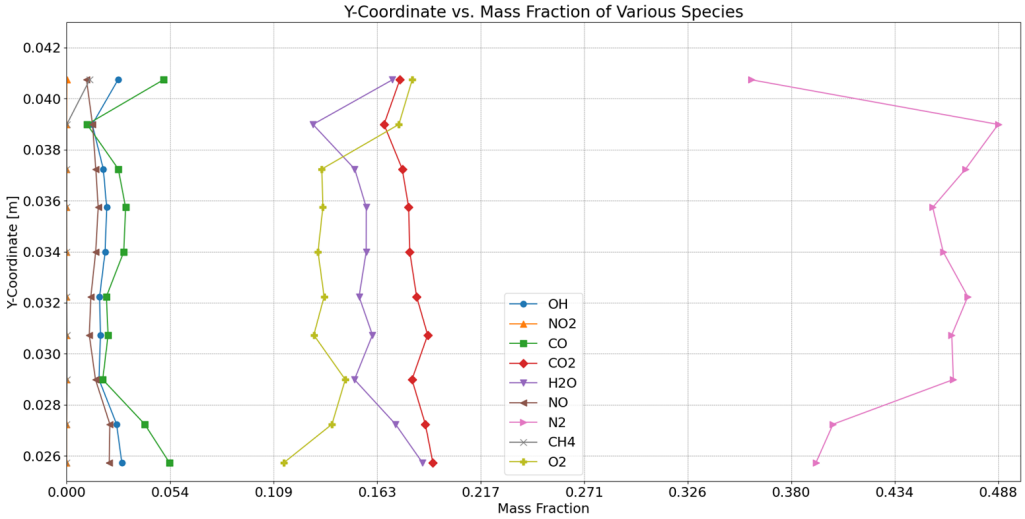


Figure 19. Species distribution on probe line 2 inside the chamber at 1 ms.

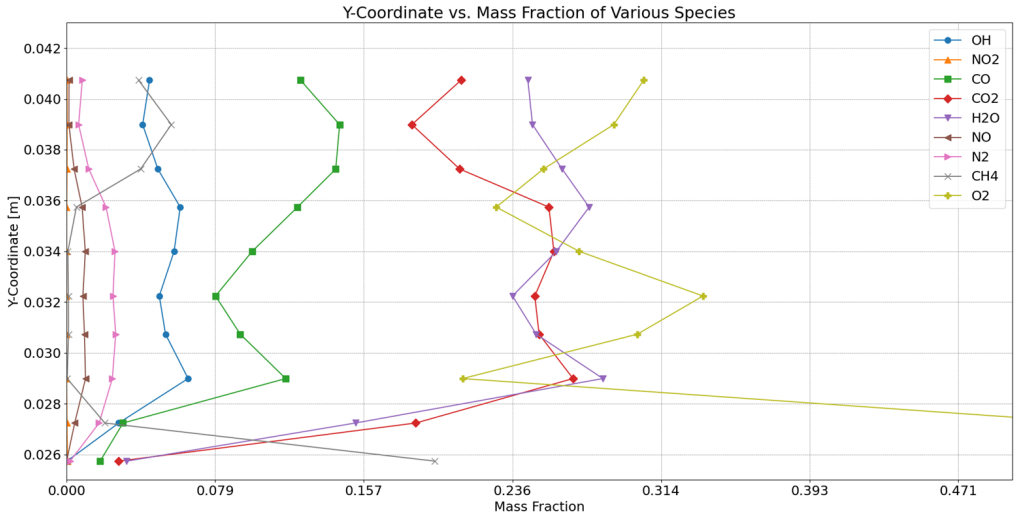


Figure 20. Species distribution on probe line 2 inside the chamber at 6 ms.

The pressure is slowly building up during the flame front propagation tending to reach the design value of 20 bar.

6. Discussion

Herein, salient features of the flame ignition and propagation processes in a rocket engine equipped with a pintle injector have been investigated. The complexity of the

numerical simulation has increased the computational burden such that only the first 6 ms of the simulation were successfully accomplished. It is acknowledged that the steady state has not been reached and probably needs 10 more milliseconds. The spark ignition as it is implemented in Ansys Fluent in the framework of the EDC model seems to overestimate the temperature rise of the burnt gases; hence, a limitation of the maximum temperature was required but only for a few time steps until the reaction mechanism has developed in a sufficient number of cells. Based on the instantaneous snapshots, for the first steps of the ignition process, a flame front velocity of about 180 m/s was estimated which is comparable with the turbulent flame velocity obtained using FGM model. The presence of air trapped inside the chamber in the initial moments of the ignition generates substantial amounts of pollutants at engine start-up. The development of NOx species outside the chamber at the interface between the hot jet and ambient air could persuade researchers to develop strategies to treat the exhaust gases to mitigate the environmental impact. The present results represent the first step in the process of pintle performance optimization, leading to a better, smoother mixing process to reduce the unburned hydrocarbons even further. The development of high quantities of carbon monoxide could mean, apart from imperfect mixing regions, that the length and/or width of the combustion chamber should be modified (most likely increased) to enhance the residence time for CO/CO_2 conversion. It becomes apparent that if this amount of CO is generated for a GCH4/GOX combustion, then, for a two-phase (GCH4/LOX) combustion, the efficiency of the burning may drop even to lower values when vaporization is to be accounted for as well. Moreover, the uneven mixing regions, temperature distribution and flame front behavior observed in the CFD analysis have a direct impact on flame stability and thermal load on the exposed parts of the injector, particularly the pintle tip. Reducing the thermal load by film cooling might be the only alternative to thermal barrier coating. The identification of these zones through numerical simulation provides a direct insight into the operation of the engine and is the starting point in the future design optimization process of the pintle injector, reducing the development costs generated by the need for iterative prototyping, at least in the early design stage.

It was noticed that the real-gas approach in the form of the Peng–Robinson equation of state, although seemingly unnecessary at first glance as pressure was moderate, showed quite consistent departures from ideal gas behavior, especially inside the pintle injector. The magnitude of this departure will increase with growing pressure and enforcing cryogenic conditions for oxidizers. Alternatively, a more complex chemistry–turbulence interaction model like the FGM model may offer better insights into the intricate ignition and flame development process. Finally, depending on the computational resources, the complexity of the model can be raised to a large eddy simulation level.

A further comparison between EDC and FGM models would probably determine which approach is better for ignition simulation.

7. Conclusions

Although the use of the GRI mechanism may be debatable as it was built to work properly in mild pressure conditions, we noticed that during the ignition process, the pressure is building up slower than the temperature for this GOX-GCH4 simulation. In this way, we can explain why we can still use it, at least for a short time during ignition, even if there are other mechanisms much better fitted to high-pressure environments.

The main insights regarding the ignition process and flame propagation of a pintle-based GOX-GCH4 rocket engine delivered in this study can be summarized as follows:

- Flame velocity propagation: the flame velocity of ~185 m/s during ignition indicates an efficient combustion initiation. This value is only a rough estimation and requires

further analysis using alternative turbulence chemistry interactions like the FGM model. The noticed short chemical timescales in the combustion chamber support this approach.

- Flame stabilization: the utilization of this type of pintle injector generates a large central recirculation system that enhances combustion stability by anchoring the flame on the lip of its end wall.
- Pollutant formation: NOx formation due to the trapped air inside the chamber during the ignition process, showing the importance of using a chamber purging mechanism in real life applications.
- Thermal load: the high thermal stress observed at the pintle tip shows the need for further design improvements on the injector geometry or film cooling to prevent material degradation during prolonged use.
- Recirculation zones: the formation of the recirculation zones provided an enhanced fuel–oxidizer mixing, increasing combustion efficiency and flame stability.
- Real-gas effects on combustion performance: deviations from ideal gas behavior were observed, emphasizing the importance of using a real gas model in moderate-to-high-pressure and high-temperature conditions.
- Recommendations for further optimization: chamber length adjustments are required for increased mixing performance and overall efficiency.

These findings provide a foundation for a more efficient alternative to the more expensive experimental iterations used for the optimization processes on rocket engines with pintle-type injectors. Further research could include alternative combinations of propellants as well as a comprehensive experimental validation for the numerical findings.

Author Contributions: Conceptualization, A.M. and D.I.; methodology, A.M.; formal analysis, D.I.; investigation, A.M.; writing—original draft, A.M.; writing—review and editing, D.I. All authors have read and agreed to the published version of the manuscript.

Funding: This research received no external funding.

Data Availability Statement: All data, models, or codes that support the findings of this study are available from the corresponding author upon reasonable request.

Conflicts of Interest: The authors declare no conflicts of interest.

References

1. Yan, D.; Wei, Z.; Xie, K.; Wang, N. Simulation of thrust control by fluidic injection and pintle in a solid rocket motor. *Aerosp. Sci. Technol.* **2020**, *99*, 105711. [CrossRef]
2. Kim, H.; Kang, H.; Kwon, S. A feasibility study of using pintle injector as sole throttling device for shallow throttling condition. *Acta Astronaut.* **2020**, *167*, 272–279. [CrossRef]
3. Yoon, W.; Yoon, H.; Ahn, J.; Ahn, K. Flow measurement and instrumentation flow control characteristics of throttling venturi valve with adjustable area. *Flow Meas. Instrum.* **2021**, *81*, 102034. [CrossRef]
4. Zhao, Z.; Cai, G.; Zhao, B.; Liu, Y.; Yu, N. Experimental investigation of a flow-oriented throttleable injector designed for throttleable hybrid rocket motor. *Acta Astronaut.* **2022**, *192*, 122–132. [CrossRef]
5. Lee, S.; Kim, D.; Koo, J.; Yoon, Y. Spray characteristics of a pintle injector based on annular orifice area. *Acta Astronaut.* **2020**, *167*, 201–211. [CrossRef]
6. Zhang, Y.; Yu, N.; Tian, H.; Li, W.; Feng, H. Experimental and numerical investigations on flow field characteristics of pintle injector. *Aerosp. Sci. Technol.* **2020**, *103*, 105924. [CrossRef]
7. Jin, X.; Shen, C.; Lin, S.; Zhou, R. Experimental study on the spray characteristics of a gas-liquid pintle injector element. *J. Vis.* **2022**, *25*, 467–481. [CrossRef]
8. Jin, X.; Shen, C.; Zhou, R.; Fang, X. Effects of LOX particle diameter on combustion characteristics of a gas–liquid pintle rocket engine. *Int. J. Aerosp. Eng.* **2020**, *2020*, 8867199. [CrossRef]

9. Liberatori, J.; Malpica Galassi, R.; Liuzzi, D.; Filosa, A.; Valorani, M.; Ciottoli, P.P. Uncertainty quantification in RANS prediction of LOX crossflow injection in methane. In Proceedings of the AIAA Propulsion and Energy Forum, Virtual, 9–11 August 2021; pp. 1–18.
10. Blanchard, S.; Cazères, Q.; Cuenot, B. Chemical modelling for methane oxy-combustion in Liquid Rocket Engines. *Acta Astronaut.* **2022**, *190*, 98–111. [CrossRef]
11. Chang, Y.; Zou, J. Experimental and Numerical Study on the Ablation Analysis of a Pintle Injector for GOX/GCH4 Rocket Engines. *Coatings* **2023**, *13*, 1022. [CrossRef]
12. Frassoldati, A.; Cuoci, A.; Faravelli, T.; Ranzi, E.; Candusso, C.; Tolazzi, D. Simplified kinetic schemes for oxy-fuel combustion. In Proceedings of the Sustainable Fossil Fuels for Future Energy—S4FE, Rome, Italy, 6–10 July 2009.
13. Zubanov, V.M.; Stepanov, D.V.; Shabliy, L.S. The technique for simulation of transient combustion processes in the rocket engine operating with gaseous fuel "hydrogen and oxygen". *J. Phys. Conf. Ser.* **2017**, *803*, 012187. [CrossRef]
14. Gerasimov, G.Y.; Shatalov, O.P. Kinetic mechanism of combustion of hydrogen–oxygen mixtures. *J. Eng. Phys. Thermophys.* **2013**, *86*, 987–995. [CrossRef]
15. Peters, N. Laminar diffusion flamelet models in non-premixed turbulent combustion. *Prog. Energy Combust. Sci.* **1984**, *10*, 319–339. [CrossRef]
16. Peters, N. Laminar flamelet concepts in turbulent combustion. *Symp. (Int.) Combust.* **1988**, *21*, 1231–1250. [CrossRef]
17. Kang, D.; Han, S.; Ryu, C.; Ko, Y. Design of pintle injector using Kerosene LOx as propellant and solving the problem of pintle tip thermal damage in hot firing test. *Acta Astronaut.* **2022**, *201*, 48–58. [CrossRef]
18. Fang, X.-X.; Shen, C.-B. Study on atomization and combustion characteristics of LOX/methane pintle injectors. *Acta Astronaut.* **2017**, *136*, 369–379. [CrossRef]
19. Son, M.; Radhakrishnan, K.; Yoon, Y.; Koo, J. Numerical study on the combustion characteristics of a fuel-centered pintle injector for methane rocket engines. *Acta Astronaut.* **2017**, *135*, 139–149. [CrossRef]
20. De Giorgi, M.G.; Sciolti, A.; Ficarella, A. Application and Comparison of Different Combustion Models of High Pressure LOX/CH4 Jet Flames. *Energies* **2014**, *7*, 477–497. [CrossRef]
21. Van Oijen, J.; De Goey, L. Modelling of Premixed Laminar Flames using Flamelet-Generated Manifolds. *Combust. Sci. Technol.* **2000**, *161*, 113–137. [CrossRef]
22. Lopes, A.V.B.; Emekwuru, N.; Abtahizadeh, E. Flamelet generated manifold simulation of highly swirling spray combustion: Adoption of a mixed homogeneous reactor and inclusion of liquid-flame heat transfer. *AIP Adv.* **2022**, *12*, 115026. [CrossRef]
23. De Giorgi, M.G.; Leuzzi, A. CFD Simulation of Mixing and Combustion in LOX/CH4 Spray Under Supercritical Conditions. In Proceedings of the 39th AIAA Fluid Dynamics Conference, San Antonio, TX, USA, 22–25 June 2009.
24. Li, Z.; Cheng, P.; Li, Q.; Cao, P. Study on the formation and maintenance mechanism of the stationary flame at the head of a LOX/GCH4 pintle injector element. *Aerosp. Sci. Technol.* **2024**, *145*, 108899. [CrossRef]
25. Shen, C.; Zhou, R. Experimental study on the combustion characteristics of LOX/LCH4 pintle injectors. *Fuel* **2023**, *339*, 126909. [CrossRef]
26. Mereu, A.; Isvoranu, D. Joint design and simulation of GOX-GCH4 combustion and cooling in an experimental water-cooled subscale rocket engine. *INCAS Bull.* **2023**, *15*, 159–167. [CrossRef]
27. Dressler, G.; Bauer, J. TRW pintle engine heritage and performance characteristics. In Proceedings of the 36th AIAA/ASME/SAE/ASEE Joint Propulsion Conference and Exhibit, Las Vegas, NV, USA, 24–28 July 2000.
28. Ponomarenko, A. RPA: Tool for Liquid Propellant Rocket Engine Analysis C++ Implementation. May 2010. Available online: http://software.lpre.de/doc.htm (accessed on 23 January 2024).
29. *Ansys® Fluent Theory Guide, Release 2022R1*; ANSYS, Inc.: Canonsburg, PA, USA, 2022.
30. Gritskevich, M.S.; Garbaruk, A.V.; Schütze, J.; Menter, F.R. Development of DDES and IDDES Formulations for the k-ω Shear Stress Transport Model. *Flow Turbul. Combust.* **2012**, *88*, 431–449. [CrossRef]
31. Lewandowski, M.T.; Ertesvåg, I.S. Analysis of the Eddy Dissipation Concept formulation for MILD combustion modelling. *Fuel* **2018**, *224*, 687–700. [CrossRef]
32. Lewandowski, M.T.; Li, Z.; Parente, A.; Pozorski, J. Generalized Eddy Dissipation Concept for MILD combustion regime at low local Reynolds and Damköhler numbers. Part 2: Validation of the model. *Fuel* **2020**, *278*, 117743. [CrossRef]
33. Smith, G.P.; Golden, D.M.; Frenklach, M.; Moriarty, N.W.; Eiteneer, B.; Goldenberg, M.; Bowman, C.T.; Hanson, R.K.; Song, S.; Gardiner, W.C.; et al. GRI-Mech 3.0. Available online: http://www.me.berkeley.edu/gri_mech/ (accessed on 14 September 2024).
34. Zimont, V. Gas Premixed Combustion at High Turbulence. Turbulent Flame Closure Model Combustion Model. *Exp. Therm. Fluid Sci.* **2000**, *21*, 179–186. [CrossRef]
35. Zimont, V.; Polifke, W.; Bettelini, M.; Weisenstein, W. An Efficient Computational Model for Premixed Turbulent Combustion at High Reynolds Numbers Based on a Turbulent Flame Speed Closure. *J. Gas Turbines Power* **1998**, *120*, 526–532. [CrossRef]
36. Zimont, V.L.; Lipatnikov, A.N. A Numerical Model of Premixed Turbulent Combustion of Gases. *Chem. Phys. Report.* **1995**, *14*, 993–1025.

37. Mouze-Mornettas, A.; Benito, M.M.; Dayma, G.; Chauveau, C.; Cuenot, B.; Halter, F. Laminar flame speed evaluation for CH_4/O_2 mixtures at high pressure and temperature for rocket engine applications. *Proc. Combust. Inst.* **2023**, *39*, 1833–1840. [CrossRef]
38. *Ansys® Fluent Theory Guide, Release 2024R1*; ANSYS, Inc.: Canonsburg, PA, USA, 2024.

Disclaimer/Publisher's Note: The statements, opinions and data contained in all publications are solely those of the individual author(s) and contributor(s) and not of MDPI and/or the editor(s). MDPI and/or the editor(s) disclaim responsibility for any injury to people or property resulting from any ideas, methods, instructions or products referred to in the content.